A bispecific monomeric nanobody induces spike trimer dimers and neutralizes SARS-CoV-2 *in vivo*

Leo Hanke[1,†], Hrishikesh Das[2,†], Daniel J Sheward[1], Laura Perez Vidakovics[1], Egon Urgard[1], Ainhoa Moliner-Morro[1], Changil Kim[1], Vivien Karl[1], Alec Pankow[1], Natalie L Smith[1], Bartlomiej Porebski[3], Oscar Fernandez-Capetillo[3,4], Erdinc Sezgin[5], Gabriel K Pedersen[6], Jonathan M Coquet[1], B Martin Hällberg[2,7,*], Ben Murrell[1,‡,*], Gerald M McInerney[1, ‡,*]

[1] Department of Microbiology, Tumor and Cell Biology, Karolinska Institutet, Stockholm, Sweden.

[2] Department of Cell and Molecular Biology, Karolinska Institutet, Stockholm, Sweden.

[3] Science for Life Laboratory, Division of Genome Biology, Department of Medical Biochemistry and Biophysics, Karolinska Institute, Stockholm, Sweden

[4] Genomic Instability Group, Spanish National Cancer Research Centre (CNIO), Madrid 28029, Spain

[5] Science for Life Laboratory, Department of Women's and Children's Health, Karolinska Institutet, Stockholm, Sweden.

[6] Center for Vaccine Research, Statens Serum Institut, Copenhagen, Denmark

[7] Karolinska Institutet VR-RÅC, Centre for Structural Systems Biology, Notkestraße 85, 22607, Hamburg, Germany

[†] Contributed equally

[‡] Contributed equally

* Correspondence to: martin.hallberg@ki.se; benjamin.murrell@ki.se; gerald.mcinerney@ki.se

Abstract

Antibodies binding to the severe acute respiratory syndrome coronavirus 2 (SARS-CoV-2) spike have therapeutic promise, but emerging variants show the potential for virus escape. This emphasizes the need for therapeutic molecules with distinct and novel neutralization mechanisms. Here we isolated a nanobody that interacts simultaneously with two RBDs from different spike trimers of SARS-CoV-2, rapidly inducing the formation of spike trimer-dimers leading to the loss of their ability to attach to the host cell receptor, ACE2. We show that this nanobody potently neutralizes SARS-CoV-2, including the B.1.351 variant, and cross-neutralizes SARS-CoV. Furthermore, we demonstrate the therapeutic potential of the nanobody against SARS-CoV-2 and the B.1.351 variant in a human ACE2 transgenic mouse model. This naturally elicited bispecific monomeric nanobody establishes a novel strategy for potent inactivation of viral antigens and represents a promising antiviral against emerging SARS-CoV-2 variants.

54 ## Introduction

55 The SARS-CoV-2 pandemic and the vast societal and economic consequences of the connected
56 lockdowns have had devastating consequences for the world's populations. Despite rapid
57 progress in vaccine development, some emerging virus variants appear to be less effectively
58 neutralized by antibodies elicited by the first-generation vaccines[1] and the emergence of further
59 variants is expected. To prepare for different scenarios and to have emergency alternatives at
60 hand, novel ways to inhibit and neutralize the virus and variants of concern are needed. As
61 therapeutic agents in the early phases of SARS-CoV-2 infection, camelid-derived single-domain
62 antibody fragments are promising candidates. These so-called 'nanobodies' not only bind their
63 antigen with very high specificity and affinity, but they can also be easily produced to large
64 quantities in *E. coli*[2] and show favorable biochemical characteristics, including good thermal
65 stability. Importantly, they can easily be combined to form homo- and heterodimers or other
66 multimers to increase potency and target multiple epitopes simultaneously[3–5]. This strategy
67 allows the neutralization of multiple known or unknown virus variants and reduces the risk for
68 viral escape[5].

69 The attachment of SARS-CoV-2 to the host cell receptor ACE2 and subsequent
70 membrane fusion is mediated by the viral spike (S) protein[6]. In the prefusion conformation, the
71 spike is a large homotrimer. Each S monomer consists of two subunits: S1 and S2. The S1
72 subunit contains the receptor binding domain (RBD) and S2 contains the fusion peptide, as well
73 as the transmembrane domain. The RBD is responsible for the initial attachment to ACE2 and is
74 found in two distinct conformational states: The receptor-accessible 'up' conformation and the
75 receptor inaccessible 'down' conformation[6,7]. Receptor binding induces the rather unstable 3-up
76 state, which leads to shedding of S1 and refolding of S2 thereby presenting the fusion peptide to
77 the opposing membrane[6,8,9]. SARS-CoV-2 is easily neutralized by high-affinity binding

78 antibodies and other spike-targeting molecules, including nanobodies[10–13]. Many of them bind to,
79 or close to, the receptor binding motif of the RBD and neutralize by directly hindering virus
80 attachment[14,15]. Other mechanisms include locking the RBDs in the down conformation or
81 preventing productive fusion[5,16]. Still, the emergence of new virus variants that evade antibody-
82 mediated neutralization mandates the identification of molecules with a more diverse set of
83 binding epitopes and neutralization mechanisms allowing for neutralization of a variety of virus
84 variants. Here, we generated a nanobody that has two non-overlapping interaction sites on the
85 SARS-CoV-2 RBD, each targeting a different epitope, which induces the formation of dimers of
86 spike trimers and rescues mice from lethal SARS-CoV-2 infection.
87

88 ## Results

89 **Isolation and characterization of a potent RBD-specific nanobody.**

90 To identify nanobodies with unique mode of neutralization, we immunized one alpaca (*Funny*)
91 with recombinant SARS-CoV-2 spike protein and RBD. We isolated RNA from peripheral blood
92 mononuclear cells and created phagemid libraries. Phage display screens with immobilized RBD
93 identified one promising nanobody, called Fu2. Since multimerization of nanobodies can
94 substantially improve virus neutralization potency[3,17], we created three different dimers
95 (illustrated in Fig. 1A): An Fu2-Fc fusion expressed in mammalian cells, a chemically linked
96 Fu2 homodimer, and thirdly, a heterodimer of Fu2 with a previously described RBD-specific
97 neutralizing nanobody Ty1[14]. Chemically-linked constructs were generated using a combination
98 of sortase A labelling and Cu-free click-chemistry as described in detail previously[3].

99 Using a pseudotyped lentivirus (PSV) neutralization assay (Fig. 1B), we found that
100 monomeric Fu2 was approximately 10-times more potent than Ty1, with an IC_{50} in the range of
101 106 ng/ml (7 nM). The Fu2-Fc fusion only slightly increased the neutralization potency of this

102 nanobody to 61 ng/ml (0.75 nM), and a chemical homo-dimerization to an IC_{50} of 26 ng/ml (0.8
103 nM). Thus, the observed enhancement in potency is attributable to dimerization, rather than the
104 Fc-domain itself. Interestingly, the Fu2-Ty1 heterodimer was extremely potent, with an IC_{50} of 4
105 ng/ml (140 pM) which is approximately 6-fold lower than that of the Fu2 homodimer. Fu2
106 directly prevented spike binding to ACE2 as confirmed by flow cytometry of HEK293T-hACE2
107 cells stained with recombinant, fluorescently labelled spike (+/- Fu2) (Fig. 1C). Analysis of
108 binding kinetics by surface plasmon resonance (SPR) revealed that Fu2 bound the RBD with
109 sub-nanomolar affinity (Fig. 1D). A 1:1 binding model fit the sensorgrams well at the used
110 concentration range, indicating a single dominant interaction. Analysis of next-generation
111 sequencing data for other members of the Fu2 lineage yielded several Fu2-variants with similar
112 properties (Figs. S1A-E).

113 To test the integrity of the recombinant spike protein after the addition of Fu2, we
114 analyzed the size-exclusion chromatography elution profiles in combination with different
115 nanobody constructs (Fig. 1E). The SARS-CoV-2 spike trimer eluted in a single peak and the
116 addition of Ty1[14] did not result in a shift in the position of this peak, which is expected given the
117 small relative size addition of the 14 kDa nanobody to the large (>400 kDa) spike trimer. In
118 contrast, the addition of Fu2 resulted in a substantial shift of the peak, suggesting the formation
119 of a larger complex, likely a dimer of the spike trimer. Next, we combined the spike with the
120 Fu2-Ty1 heterodimer. This also resulted in earlier elution, and besides a possible spike dimer,
121 this construct gave rise to an even earlier elution peak suggesting the induction of higher-order
122 spike multimers.

123 To test if the Fu2-induced multimerization of spike also occurs when it is presented
124 on virus particles, we analyzed GFP-labeled SARS-CoV-2 pseudotyped lentiviruses (PSV-GFP)
125 after addition of the nanobodies Ty1 or Fu2 (Fig. 1F). To this end, we performed fluorescence

126 correlation spectroscopy and measured apparent brightness of each diffusing particle. The
127 majority of single diffusing particles preincubated with Fu2 showed a 2.5-fold increase in
128 brightness compared to PSV-GFP alone or preincubated with Ty1, suggesting that Fu2 leads to
129 aggregation of the PSV-GFP particles.
130
131 **Structural basis for the induction of spike trimer dimers by Fu2.**
132 To better understand neutralization and the aggregation of spike by Fu2, we used electron
133 cryomicroscopy (cryo-EM) to determine the structure of the Fu2-spike complex. The structure
134 revealed a remarkable head-to-head dimerization of the trimeric spike, bound by six molecules of
135 Fu2 (Fig. 2). This distinct structural state appeared as prominent 2D classes in our analyses (Fig.
136 2A). Binding of Fu2 to the RBD is unique as it can simultaneously interact with two different
137 RBDs from different spike trimers in the up conformation (Figs. 2B and 2C). To our knowledge,
138 Fu2 is the only nanobody or spike-binding molecule developed against the SARS-CoV-2 spike
139 to have this property. Our high resolution (2.9Å; 0.143 FSC) localized reconstruction of the
140 RBD-Fu2-RBD-Fu2 interface helped us elucidate the molecular details of this interaction. Each
141 RBD in the complex provides two binding interfaces for two Fu2 molecules, which we call
142 'interface-major' and 'interface-minor' according to surface area covered (Figs. 2D, S2A and
143 S2B). The interface-major and interface-minor have a buried surface area of ~740 $Å^2$ and
144 ~495 $Å^2$, respectively. Parts of the Fu2 framework regions drive the dimerization by shape-
145 complementarity and coupled solvent exclusion in the two interfaces. In addition, the interface-
146 major consists of 15 hydrogen bonds and one salt bridge between Fu2 D117 and RBD K378,
147 while the interface-minor comprises five hydrogen bonds. Furthermore, a region around the Fu2
148 β-turn A40-K43 plays a key role in dimerization through interactions with two proximal RBDs
149 (Figs. S2C and S2D). Specifically, one of the two proximal RBDs' T500-Y505 region packs

150 against the Fu2 A40-K43 β-turn and the RBD Y505 is in addition bound by Fu2 Q39.
151 Meanwhile, the other proximal RBD is bound through a bidentate hydrogen bond between Fu2
152 E44 and the backbone amides of RBD V503-G504 (Figs. 2E, S2C and S2D). Interestingly, the
153 overall structure of Fu2-bound spike had no significant deviations from previous structures (Fig.
154 S3), and we did not find any contact between any two Fu2 molecules or between spike trimers
155 suggesting that the observed spike trimer dimerization is solely driven RBD-Fu2 interactions.
156

157 **Fu2 blocks the RBD from binding ACE2.**

158 Structural alignment of an ACE2-RBD structure (PDB: 6LZG[18]) to the Fu2-spike structure
159 (single RBD) shows that binding of ACE2 would be hindered by Fu2 bound to any of the two
160 interfaces (Fig. 2F). Fu2 bound to the interface-major would clash with ACE2 residues ~303-331
161 and the N-glycan at position 322, while Fu2 bound to interface-minor would mask the interaction
162 surface of ACE2, making it sterically impossible for ACE2 to access the RBD. A comparison of
163 the Fu2 and Ty1 binding site revealed that interface-minor is partially shared between Ty1 and
164 Fu2 (Figs. S2E and S2F), suggesting that in context of the Fu2-Ty1 heterodimer, Ty1 is
165 displaced upon dimerization of the spike trimer. Ty1 can then potentially bind additional spike
166 molecules, explaining the elution profile showing both dimers and higher order spike complexes
167 (Fig. 1E).
168 In the complex, Fu2's long CDR3 (G99 to Y120) plays a significant role in RBD binding. Here,
169 the Fu2 S107-R111 region adopts a β-strand conformation that binds the RBD T376-Y380 β-
170 strand to give rise to an energetically favorable inter-chain extension of the RBD anti-parallel β-
171 sheet (Figs. 2G and 2H). Interestingly, the Fu2 CDR1 (G26-Y32) and CDR2 (T52-S57) do not
172 participate in RBD binding, and none of the CDRs is directly involved in the formation of the
173 spike dimer.

174

175 **Fu2 stabilizes the RBD in the 'up' conformation.**

176 Cryo-EM analyses, both of the purified spike or of intact virions, have revealed that unliganded
177 spike is mostly present in all-down (~60%) or 1-up (~40%) conformation[6]. Our Fu2-spike
178 structure shows the presence of two trimeric spike molecules, both in the 3-up conformation.
179 This arrangement allows Fu2 to access all six possible binding sites on RBDs without steric
180 conflict. Alignment of RBD-Fu2 to RBD-down in a 2-up spike structure confirms that binding of
181 Fu2 to RBD in the down conformation is not possible (Fig. S2G). Fu2 bound to either interaction
182 interface on an RBD in the down conformation would clash with neighboring RBDs. Likewise,
183 an alignment of the 2-up spike structure to the Fu2-trimer-dimer shows that RBD-down would
184 clash with the neighboring Fu2 molecule (Fig. S2H). In conclusion, for Fu2 binding and for
185 trimer-dimer assembly, all RBDs must be in the up conformation.

186

187 **Fu2 cross-neutralizes SARS-CoV, and clinical isolates of SARS-CoV-2 including the**
188 **B.1.351 variant of concern**

189 To test the breadth of neutralization, we evaluated cross-neutralization of SARS-CoV PSV (Fig.
190 3A). While Ty1 did not neutralize SARS-CoV, Fu2 and dimeric Fu2 constructs were
191 neutralizing, but less so than against SARS-CoV-2 PSV. Interestingly, the neutralization curves
192 displayed a much flatter slope as compared to those against SARS-CoV-2 PSV. It required 6.1
193 μg /ml of monomeric Fu2 to reach 50% neutralization in this assay, while 570 ng /ml of Fu2-Fc
194 and 57 ng/ml of the Fu2-dimer was sufficient for 50% neutralization.

195 To understand the molecular mechanism of cross-neutralization of SARS-CoV we
196 compared the RBD sequences and performed structural alignments (Figs. 3B, 3C and S4A).
197 Interestingly, the interface-major residues are conserved, while interface-minor has significant

198 differences, suggesting that the divergent interface-minor of SARS-CoV RBD would not permit
199 Fu2 binding. From these analyses we conclude that Fu2 would be unlikely to induce SARS-CoV
200 trimer dimers.

201 To demonstrate neutralization of replication competent SARS-CoV-2 we
202 performed a plaque reduction neutralization test (PRNT) using infectious SARS-CoV-2, isolated
203 from the first Swedish COVID-19 patient[19] (Fig. 3D). Similar to neutralization of PSV,
204 monomeric Fu2 neutralized SARS-CoV-2 much better than Ty1, a dimeric construct of Fu2
205 provided a 2.8-fold improvement over the monomeric version of Fu2, while the heterodimer of
206 Ty1 and Fu2 showed a 50-fold improvement compared to monomeric Fu2 in this assay.

207 A PRNT using the B.1.351 (501Y.V2) variant[1] showed that Fu2 very potently
208 neutralized this variant (Fig. 3E) and that the Fu2 dimer and Fu2-Fc again improved
209 neutralization efficiency. The IC_{50} values were even slightly better than when using the Swedish
210 isolate, but the difference is within the intraassay variability. Ty1 failed to neutralize this virus,
211 and the Fu2-Ty1 heterodimer did not neutralize better than Fu2 alone. The variant B.1.351
212 harbors four amino acid substitutions in the RBD at position K417N, N439K, E484K and
213 N501Y. Only N501 and E484 are in proximity of the Fu2 interaction interface. *In silico* analyses
214 with the PISA server (25) confirmed that the two interfaces do not change in these mutants. Both
215 buried surface areas of the interfaces as well as the number of possible hydrogen bonds remain
216 unchanged (Fig. 3F). These results and analysis combined suggests that Fu2 likely also
217 neutralizes the recently emerged variants P1 (K417T, E484K, N501Y) and B.1.1.7 (N501Y).
218

219 **Therapeutic efficacy of Fu2 in a mouse model of SARS-CoV-2 infection**

220 An important requirement for the development of antivirals is neutralization potential *in vivo*. To
221 address this, we used K18-hACE2 transgenic mice that express human ACE2 as a model for

222 SARS-CoV-2 infection. To determine if Fu2 could reduce disease severity when administered in
223 early infection, we tested its ability to neutralize the virus and protect mice from signs of disease
224 *in vivo* (Fig. 4). When the Fu2-Ty1 heterodimer was administered prophylactically or
225 therapeutically, we noted that it slightly delayed the onset of disease (Fig. S7). A major issue
226 with using nanobodies therapeutically is their short half-life *in vivo*. To extend serum half-life,
227 we fused Fu2 to the nanobody Alb1 that binds mouse serum albumin[20]. Mice were challenged
228 with a standardized dose (2.4×10^6 RNA copies) of either a Swedish isolate of SARS-CoV-2 (86
229 plaque forming units, PFU) or the B.1.351 variant (100 PFU). On days 1, 3, 5 and 6 post
230 infection, mice were injected intraperitoneally (i.p.) with 600 µg of the Fu2-Alb1 heterodimer
231 (Fig 4A). All control untreated mice experienced considerable weight loss within the first week
232 of infection, with mice infected with B.1.351 experiencing a slightly faster onset of weight loss.
233 In contrast, Fu2-Alb1 delayed disease onset and protected mice from severe weight loss
234 following infection with either the wild-type or B.1.351 virus (Fig. 4B and 4C). Quantification of
235 genomic and subgenomic SARS-CoV-2 E-gene at day 5 also demonstrated that Fu2-Alb1
236 reduced viral loads, most clearly in mice infected with wild-type virus (Fig. 4D). Thus, Fu2 is a
237 suitable candidate for antiviral therapy against SARS-CoV-2 and common variants.
238

239 ## Discussion

240 Nanobodies represent a valuable alternative to monoclonal antibodies for virus
241 neutralization[21,22]. Their ease of production, thermal stability, and robust biochemical behavior,
242 combined with straight-forward functionalization and multimerization possibilities, make them
243 suitable candidates for therapeutic applications.

244 The newly emerged SARS-CoV-2 B.1.351 variant shows nine amino acid changes
245 in the spike protein. While biological properties of this variant remain to be determined, two

246 amino acid substitutions in the receptor binding motif are of potential concern for vaccine
247 efficacy, neutralization efficiency of existing monoclonal antibody therapies, and altered
248 dynamics of virus spread[23–25]. The novel nanobody described here, Fu2, can effectively
249 neutralize the B.1.351 variant and therefore has a strong and unique potential to form the basis
250 for development of therapeutic interventions against this emerging variant of concern.

251 Fu2 is also capable of neutralizing SARS-CoV, highlighting its specificity for a
252 more conserved epitope. However, the potency was significantly reduced for the monomeric
253 nanobody, likely because of decreased affinity to the RBD of this virus. That the dimeric
254 constructs significantly increased potency further supports this hypothesis. A similar observation
255 was made for VHH-72 originally developed against SARS-CoV, but with some neutralization
256 potential in dimeric form against SARS-CoV-2[26,27].

257 Nanobodies typically have short serum half-lives, ranging from 1-3 hours[28],
258 compared to 6-8 days of IgG1[29]. This characteristic can dramatically influence applicability for
259 virus neutralization. Accordingly, for a Fu2-Ty1 heterodimer, we could not detect any protective
260 effect when administered prophylactically, while therapeutic administration significantly delayed
261 disease onset and severity (Fig. S7). In contrast, a half-life extended Fu2-Alb1 heterodimer
262 showed therapeutic efficacy against 'wild-type' and B.1.351 (Fig. 4), suggesting that nanobody-
263 based constructs have the potential for SARS-CoV-2 antiviral therapy.

264 The RBD-specific nanobody Fu2 displays a particularly unique mode of virus
265 neutralization by rapidly inducing stable spike trimer dimers that are incapable of binding to
266 ACE2. In contrast to spike trimer dimers reported for the full-length spike that are based on S1-
267 S1 interactions placing the trimers 'side-by-side'[30], Fu2 induced a dimer in a 'head-to-head'
268 orientation with the C-termini at the distal ends. Targeting two epitopes increases the binding
269 surface area, but, more importantly, when locked in such a conformation the function of each

spike is sterically blocked both by the nanobody and by the other spike in such a way that the whole complex must dissociate for the spike to regain its function.

The interaction between Fu2 and the RBD is highly unusual, and for a monomer to induce antigen dimerization in this manner, two copies of an antigen must be bound at different epitopes with precisely the right spatial arrangement. This novel mode of antigen binding may be uncommon in naturally elicited antibody repertoires but could be achievable by structure-based antibody design and might present a general strategy for potent immobilization of viral glycoproteins and other antigens. It remains to be seen whether 'designer' bispecific monomeric nanobodies can push the potency envelope beyond what is currently attainable.

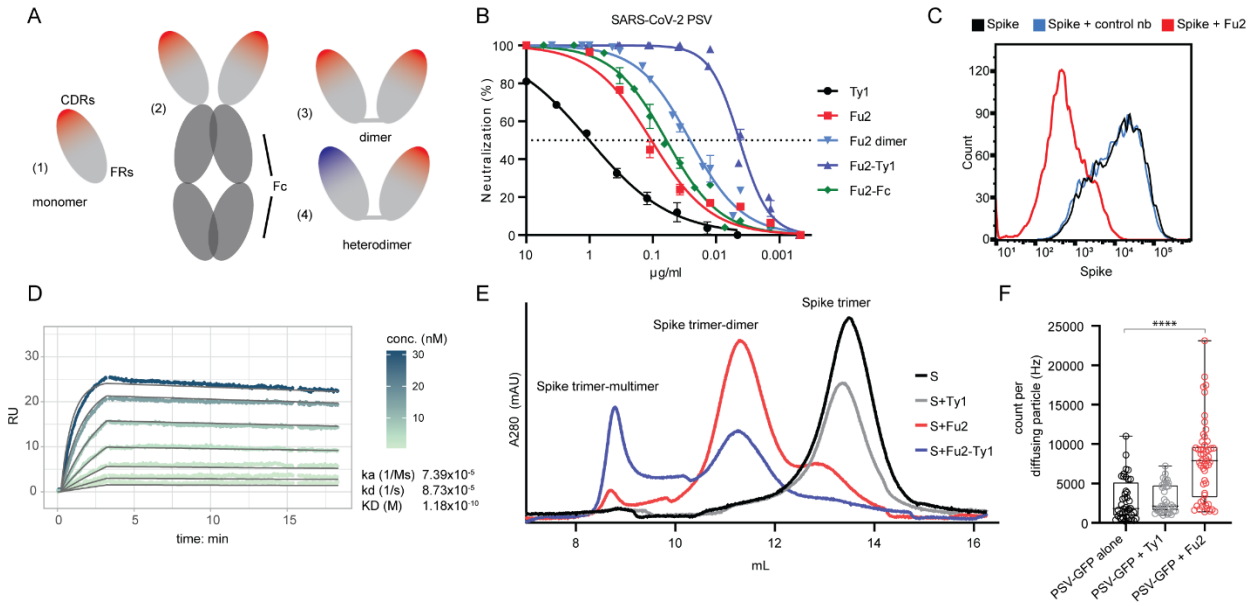

Fig. 1. An RBD-specific nanobody neutralizes SARS-CoV-2. (**A**) Overview of different nanobody constructs used in this study: (1) nanobody monomer, (2) nanobody Fc-fusion, (3) chemically linked nanobody homodimer, (4) chemically linked nanobody heterodimer. (**B**) A SARS-CoV-2 spike pseudotyped lentivirus (PSV) was incubated with a dilution series of the indicated nanobodies at 37°C for one hour before infecting HEK293T-hACE2 cells. Neutralization (in %) compared to untreated PSV is shown. Data from at least two replicates is shown and the error bars represent the standard deviation. (**C**) Recombinantly expressed, prefusion stabilized, and fluorescently labelled SARS-CoV-2 spike protein was incubated with a control nanobody specific for IAV NP[31], or Fu2 and used to stain ACE2 expressing HEK293T cells. Cells were analyzed by flow cytometry and a representative histogram is shown. (**D**) Binding kinetics of Fu2 to the RBD were measured by surface plasmon resonance (SPR). Sensorgram is color-coded based on concentration. The fit is based on the 1:1 Langmuir model

292 and is shown in dark grey solid lines. (**E**) Recombinantly expressed, prefusion stabilized SARS-
293 CoV-2 spike protein was run alone or preincubated with the indicated nanobody constructs on a
294 Superose 6 size-exclusion column. Elution profiles (A280) are shown. (**F**) GFP-labelled SARS-
295 CoV-2 spike pseudotyped lentivirus (PSV-GFP) was incubated with Ty1, Fu2 or left alone and
296 brightness of diffusing virus particles was quantified using fluorescence correlation spectroscopy
297 in solution. Statistical significance was evaluated using Kolmogorov-Smirnov test.

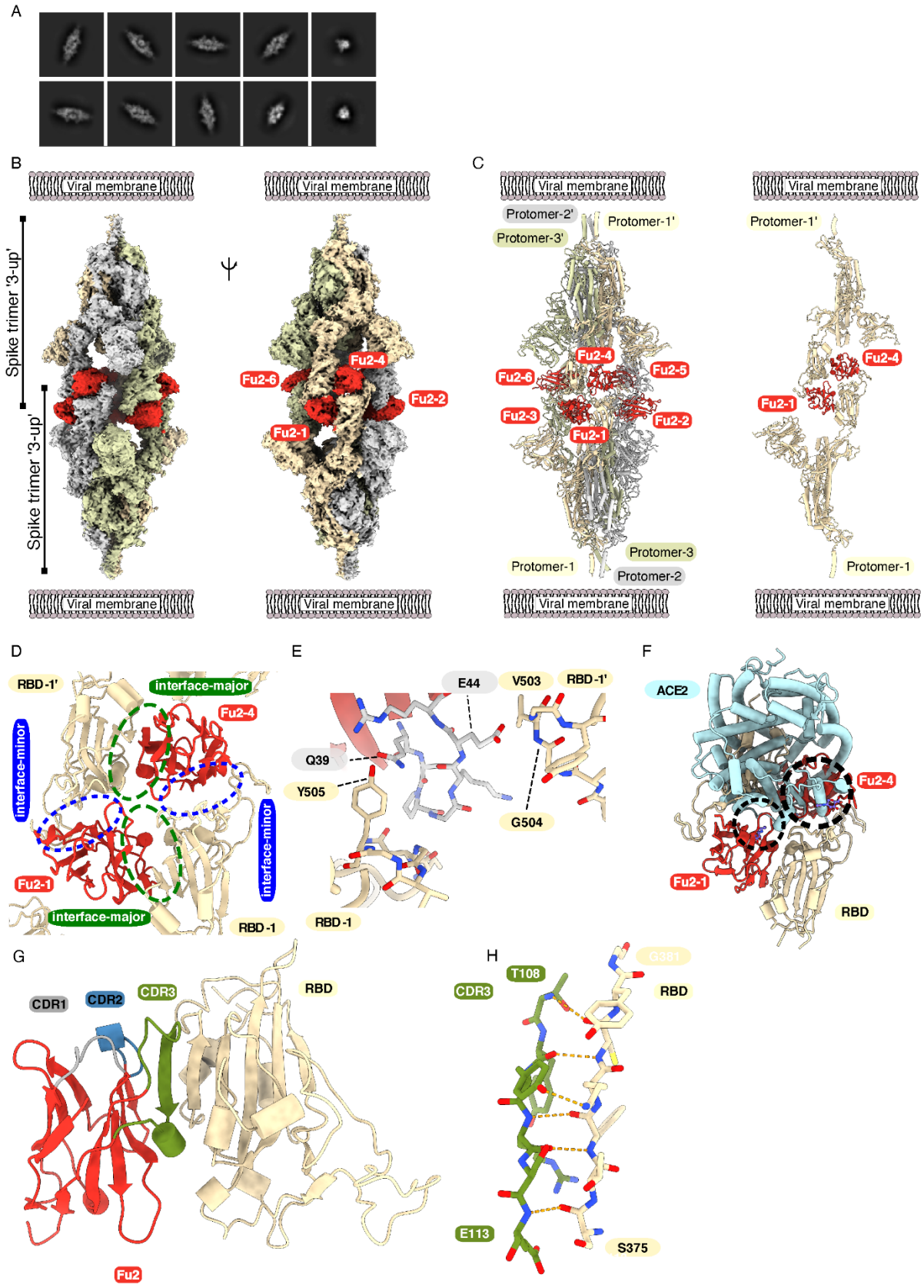
A
B
Viral membrane
Spike trimer '3-up'
Spike trimer '3-up'
Fu2-4
Fu2-6
Fu2-2
Fu2-1
C
Protomer-2'
Protomer-1'
Protomer-3'
Fu2-4
Fu2-6
Fu2-5
Fu2-3
Fu2-2
Fu2-1
Protomer-3
Protomer-1
Protomer-2
Protomer-1'
Fu2-4
Fu2-1
Protomer-1
D
RBD-1'
interface-major
Fu2-4
interface-minor
interface-minor
Fu2-1
interface-major
RBD-1
E
E44
V503
RBD-1'
Q39
Y505
G504
RBD-1
F
ACE2
Fu2-4
Fu2-1
RBD
G
CDR1
CDR2
CDR3
RBD
Fu2
H
T108
CDR3
RBD
E113
S375

298

Fig. 2. Cryo-EM provides structural evidence of Fu2-mediated dimerization of trimeric spike in '3-up' conformation (**A**) Representative 2D class averages. (**B**) Cryo-EM map (two different side views) and (**C**) Atomic model of 'dimeric' spike in complex with Fu2; and two opposite protomers with two Fu2 molecules. Both spike trimers in the complex are present in '3-up' conformation (six Fu2 molecules are numbered). (**D**) Close-up view of the RBD-Fu2 interaction interfaces showing the interface-major and interface-minor. (**E**) A β-hairpin (gray sticks) from the Fu2 framework region (residues 39-45) contacts two RBDs simultaneously in the Fu2-mediated spike trimer-dimer. (**F**) Modelling of simultaneous spike-Fu2-ACE2 binding shows that Fu2 blocks the binding of ACE2 (PDB:6LZG)[18] to the RBD from two directions. Clashes marked with dashed circles. (**G**) Fu2 binds the RBD through an extended inter-chain β-sheet interaction mediated by the CDR3 region (green). CDR1 (gray) and CDR2 (blue) does not take part in RBD binding (**H**) Closeup of a part of the CDR3-RBD interface displaying the anti-parallel β-strand hydrogen bond pairing between the Fu2 CDR3 region and the RBD (light orange).

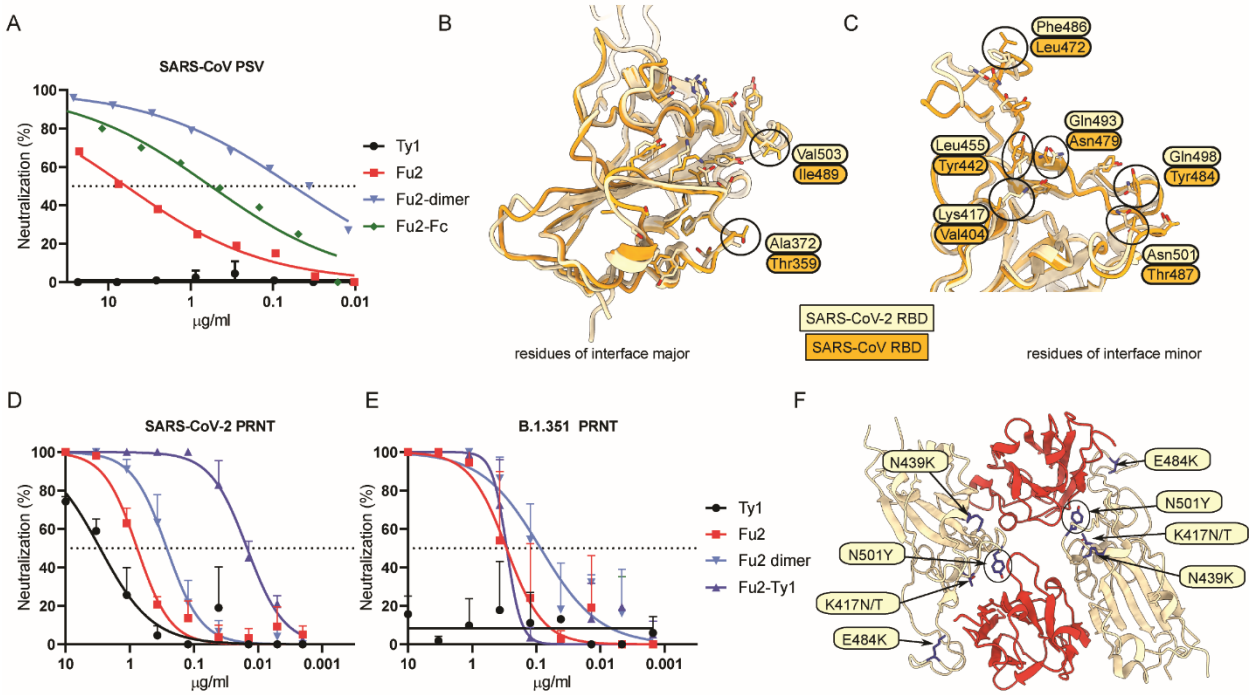

Fig. 3. Fu2 cross-neutralizes SARS-CoV and a B.1.351 variant of concern clinical isolate (**A**) SARS-CoV S pseudotyped lentivirus (PSV) was incubated with the indicated constructs before infecting HEK293T-ACE2 cells, and neutralization is shown compared to untreated PSV. (**B** and **C**) Structural basis of SARS-CoV cross-neutralization by Fu2. Structural alignment of SARS-CoV-2 Spike (RBD bound Fu2) with SARS-CoV RBD (PDB:6ACD)[32]. Residues of interface-major and interface-minor shown as sticks, divergent residues are labelled. (**D and E**) PRNTs with clinical isolates of SARS-CoV-2. 100 plaque forming units (PFU) of SARS-CoV-2[19] or B.1.351 (501Y.V2)[1] were incubated with dilution series of the indicated nanobody constructs for 1 h at 37°C before infecting monolayers of Vero E6 cells. Plaques were quantified 72 h post infection. Neutralization representing the reduction of plaques relative to the control wells is shown. Error bars represent standard deviation (SD) across replicate experiments. (**F**) Assessment of Fu2-RBD interaction in RBD variants. *In silico* mutational analyses of RBD residues and probable impact on Fu2 binding. Fu2 is shown in red and variant residues are indicated.

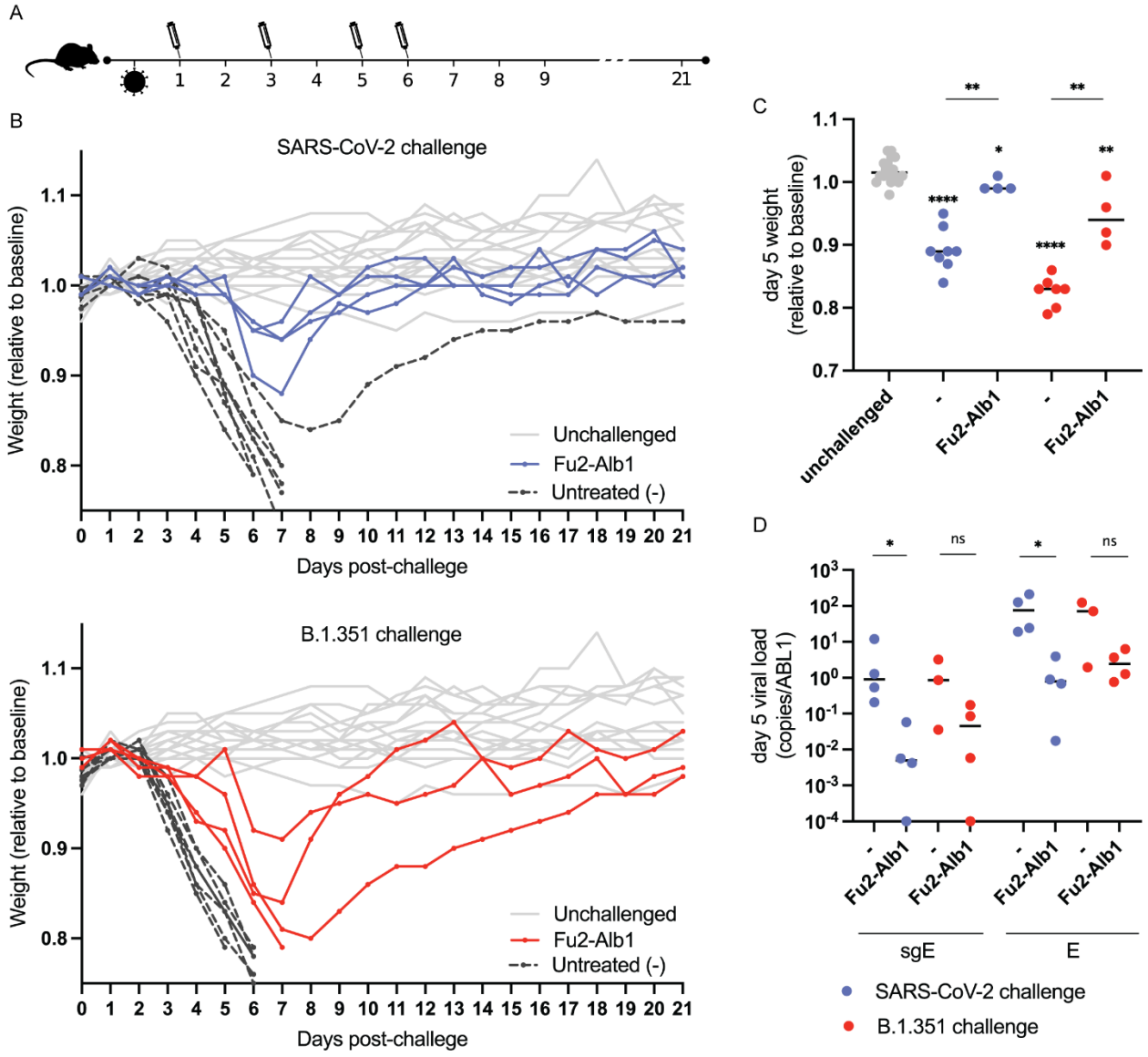

Fig. 4. Therapeutically administered nanobody rescues mice from lethal SARS-CoV-2 infection.

(**A**) Timeline of the challenge experiment. K18-hACE2 transgenic mice were challenged with 86 PFU of SARS-CoV-2 (blue, 'wild-type') or 100 PFU of B.1.351 (red) and injected with Fu2-Alb1 (half-life extended Fu2) at indicated time points. (**B**) Weight of mice during the challenge experiment. The mean weight of each mouse of day 0 to day 2 served as baseline and the weight loss relative this baseline is shown. Uninfected mice are shown in grey, untreated infected mice in black. Half of the untreated mice are historical controls from identical, previously conducted experiments. The weight for the same unchallenged control mice is shown in the upper and lower panel. (**C**) Weight loss for day 5 for each group. (**D**) Analysis of oropharyngeal samples from mice at day 5 in infected groups. Ratios of E-gene to ABL1 is shown for both genomic and subgenomic RNA. Statistical comparisons are summarized as: *, $p \leq 0.1$; **, $p \leq 0.01$; **** $p \leq 0.0001$; ns, not significant. Groups displaying significant weight loss compared to uninfected mice are annotated above the points for that group.

357

358 **Materials and Methods**

359

360 **Cells and viruses**

361 HEK293T cell (ATCC-CRL-3216 and ATCC CRL-11268) and Vero E6 cells (ATCC-CRL-
362 1586) were maintained in DMEM (Gibco) supplemented with 10% fetal calf serum and 1%
363 penicillin-streptomycin in a humidified incubator with 5% CO_2 at 37°C. Calu-3 cells were
364 additionally supplemented with nutrient mixture F12 (Thermo Fisher Scientific). The HEK293T
365 cell line was further engineered to overexpress human ACE2 by lentiviral transduction[14]. All cell
366 lines used for the experiments were negative for mycoplasma as determined by PCR.
367 Infectious SARS-CoV-2[19] and the B.1.351[1] isolate used for PRNTs and the challenge experiment
368 in Fig. S7 were propagated in Vero E6 cells and titrated by plaque assay. Viruses used for the
369 challenge in Fig. 4 were propagated in Calu-3 cells, quantified by qPCR, and titrated by plaque
370 assay in Vero E6 cells. Challenge stocks for experiments shown in Fig. 4 were confirmed by
371 Sanger sequencing to harbor no high frequency cell culture adaptation mutations in spike.

372

373 **Proteins and probes**

374 The plasmid for the expression of the SARS-CoV-2 prefusion-stabilized spike (2P) ectodomain
375 was a kind gift from the McLellan lab[6]. The plasmid was used for transient transfection of
376 FreeStyle 293F cells using the FreeStyle MAX reagent (Thermo Fisher Scientific). The spike
377 trimer was purified from filtered supernatant on Streptactin XT resin (IBA Lifesciences) or Ni-
378 NTA resin and purified by size-exclusion chromatography on a Superdex 200 (Cytiva). For cryo-
379 EM a similar construct with 6 proline substitutions (S6-P) was used[33], and the protein was
380 purified on His-Pur Ni-NTA resin (Thermo Fisher Scientific) followed by size-exclusion

381 chromatography. The RBD domain was cloned upstream of a sortase A motif (LPETG) and a
382 6xHIS tag. The plasmid was used for transient transfection of FreeStyle 293F cells as described
383 above. The protein was purified from filtered supernatant on His-Pur Ni-NTA resin followed by
384 size-exclusion chromatography on a Superdex 200. The albumin binding nanobody Alb1 was
385 described earlier[20] and the sequence was obtained from WO/2006/122787. Nanobodies were
386 cloned in the pHEN plasmid with a C-terminal sortase motif (LPETG) and a 6xHIS tag. BL21 *E.*
387 *coli* were transformed with this plasmid, and expression was induced with 1 mM IPTG at OD600
388 = 0.6 and cells were grown overnight at 30 °C. Nanobodies were retrieved from the periplasm by
389 osmotic shock and purified on Ni-NTA resin and size-exclusion chromatography.
390 Sortase A 5M was produced as described before in BL21 *E. coli* and purified by Ni-NTA and
391 size exclusion chromatography[3]. Fluorescent spike ectodomain was generated by first attaching
392 dibenzocyclooctyine-*N*-hydroxysuccinimidyl ester (DBCO-NHS) to the spike trimer in a 3:1
393 molar ratio, before attaching AbberiorStar-635P-azide by click-chemistry. The final product was
394 purified from unreacted DBCO and fluorophore on a PD-10 desalting column. The biotinylated
395 RBD was generated using sortase A and amine-PEG3-biotin as a nucleophile. The reaction was
396 performed with 50 µM RBD, 5 µM sortase A 5M, and 8 mM amine-PEG3-biotin in 50 mM Tris
397 pH 7.5, 150 mM NaCl, for 6 hours at 4 °C. Sortase A and unreacted RBD was removed on Ni-
398 NTA resin and excess nucleophile was removed by two consecutive purifications on PD-10
399 desalting columns.
400
401 **Alpaca immunization, library generation and nanobody isolation.**
402 One adult female alpaca (*Funny*) at PreClinics, Germany, was immunized four times in a 60-day
403 immunization schedule. Each immunization consisted of two injections. For the first
404 immunization, 200 µg of prefusion stabilized spike and 200 µg of S1+S2 domain (Sino

405 Biologicals) was used. Remaining immunizations each consisted of one injection with 200 µg
406 RBD and one injection with 200 µg prefusion stabilized spike, both produced in Freestyle 293F
407 cells as described above. Serum from the final bleed at day 60 neutralized SARS-CoV-2
408 pseudoviruses with an ID50 >20 000. The animal study protocol was approved by the PreClinics
409 animal welfare officer commissioner and registered under the registration No. 33.19-42502-05-
410 17A210 at the Lower Saxony State Office for Consumer Protection and Food Safety—LAVES
411 and is compliant with the Directive 2010/63/EU on animal welfare. The nanobody phage library
412 was generated as described[14]. Phage display was performed on RBD immobilized on magnetic
413 beads.
414
415 **Dimer generation using click chemistry**
416 To generate homo- and hetero-dimers, the different nanobodies were first site-specifically
417 functionalized on the C-terminus using sortase A with either an azide or a dibenzocyclooctine
418 (DBCO) as described in detail here[3]. In brief, for functionalization with DBCO, 70 µM of
419 nanobody was incubated with 5 µM sortase A, 8 mM DBCO-amine (Sigma-Aldrich) in 150 mM
420 NaCl, 50 mM Tris pH 7.5 and 10 mM $CaCl_2$ for 3 h at 25 °C. To functionalize the nanobody
421 with an azide, 70 µM of nanobody, was incubated with 5 µM sortase A 5M, 10 mM 3-azido-1-
422 propanamine (Sigma-Aldrich #762016) in 150 mM NaCl, 50 mM Tris pH 7.5 and 10 mM $CaCl_2$
423 for 3 h at 25 °C. In both reactions, unreacted nanobody, sortase A and excess nucleophile were
424 removed using Ni-NTA resin and PD-10 columns or size-exclusion chromatography. The click
425 reaction was initiated by mixing azide and DBCO labeled nanobody in a 1:1 molar ratio for 48 h
426 at 4 °C. Dimers were purified from unreacted monomeric nanobody by size-exclusion
427 chromatography on a Superdex S200 16/600 column (Cytiva).
428

429 **Neutralization assays**

430 Pseudotyped virus neutralization assay: Pseudotyped viruses were generated by co-transfection
431 of HEK293T cells with plasmids encoding firefly luciferase, a lentiviral packaging plasmid
432 (Addgene cat#8455), and a plasmid encoding either the SARS-CoV or SARS-CoV-2 spike
433 protein, both harboring a C-terminal truncation of 18 amino acids. Media was changed 12-16 h
434 post-transfection, and pseudotyped viruses were harvested at 48 and 72 hours, filtered through a
435 0.45 µm filter and stored at -80 °C until use. Pseudotyped viruses sufficient to generate 100,000
436 relative light units (RLU) were incubated with serial dilutions of nanobody for 60 min at 37 °C.
437 15,000 HEK293T-ACE2 cells were then added to each well, and the plates were incubated for 48
438 h at 37 °C. Luminescence was measured using Bright-Glo (Promega) on a GM-2000
439 luminometer (Promega) with an integration time of 0.3 s.

440 Plaque reduction neutralization test: One day before the experiment, 100,000 Vero E6 cells were
441 seeded per well of a 24-well plate. A 3-fold serial dilution of the nanobody constructs starting at
442 10 µg/ml were incubated with 100 plaque-forming units (PFU) of the first Swedish clinical
443 isolate of SARS-CoV-2 or variant B.1.351 for 1 h at 37°C. The nanobody-virus mixture was then
444 added to the cells and incubated at 37 °C for 1 h. Cells were washed with PBS, and an overlay of
445 1% CMC/DMEM supplemented with 2% FBS was pipetted into the wells. Three days post-
446 infection, cells were fixed in 10% formaldehyde, followed by staining with crystal violet.
447 Plaques were counted and inhibition determined by comparing to control wells on the same
448 plate.

449

450 **Flow cytometry**

451 HEK293T-hACE2 cells were trypsinized and fixed in 4% formaldehyde in PBS for 20 min. Cells
452 were stained with spike-AbberiorStar-635P not premixed or premixed with Fu2 or control

453 nanobody. Fluorescence was quantified using a BD FACSCelesta and the FlowJo software
454 package.
455
456 **Surface plasmon resonance**
457 Binding kinetics were determined by surface plasmon resonance using a Biacore 2000. All
458 experiments were performed at 25 °C in a running buffer of 10 mM HEPES, 150 mM NaCl, pH
459 7.4, and 0.005% Tween-20 (v/v). Site-specifically biotinylated RBD was immobilized on
460 streptavidin sensor chips (Series S sensor Chip SA, GE Healthcare) to a level of ~200 resonance
461 units (RU). A 2-fold dilution series of the nanobodies was injected at a flow rate of 30 µl/min
462 (association 180 s, dissociation 900 s), and the immobilized RBD was regenerated using 0.1 M
463 glycine-HCL buffer pH 2 for 2x 10 seconds. Data were analyzed using BIAevaluation Software
464 and fitted using the 1:1 Langmuir model with mass transfer.
465
466 **Next generation sequencing**
467 Next generation sequencing on pre- and post-enrichment nanobody libraries was performed as
468 described in Hanke et al. 2020[14] on an Illumina MiSeq.
469
470 **Gel-filtration shift assays**
471 For the gel-filtration shift assay, 80 µg of prefusion stabilized spike protein was incubated with
472 or without nanobody for 15 minutes and was run on a Superose 6 increase 10/300 GL (Cytiva),
473 and absorbance at 280 nm was detected. Sample and injection volumes were kept identical
474 between runs to obtain comparable elution profiles.
475
476 **Fluorescent pseudotyped lentivirus brightness measurements**

477 To generate fluorescent lentiviral particles enveloped with the spike protein of the SARS-CoV-2
478 coronavirus (PSV-GFP), HEK 293T cells were reverse-transfected with 3 plasmids: psPAX2 (a
479 gift from Didier Trono, Addgene #12260), pEGFP-Vpr (obtained through the NIH HIV Reagent
480 Program, Division of AIDS, NIAID, NIH: pEGFP-Vpr, ARP-11386, contributed by Dr. Warner
481 C. Greene) and pCMV14-3X-Flag-SARS-CoV-2 S (a gift from Zhaohui Qian, Addgene #145780)
482 at 1:0.5:2 molar ratio using Lipofectamine™ 2000 (0.6 ul per 1 ug DNA; Invitrogen™, 11668019);
483 growth medium was refreshed 16 h after transfection. Virus-rich supernatant was collected twice
484 over the next 48 h and, if needed, stored at 4 °C prior to the concentration. Supernatants were
485 pooled, mixed with the Lenti-X™ Concentrator (Takara Bio, 631231) at 3:1 ratio (v:v) and
486 incubated overnight at 4 °C. The solution was then spun down at 1'500 x g for 45 min at RT, the
487 pellet was resuspended in sterile 1x PBS (Sigma-Aldrich, D8537) and stored at -80 °C.
488 PSV-GFP was incubated with 100 µg/ml Ty1, Fu2 or PBS as control for 1 h. The mixtures were
489 transferred to an 8-well glass bottom Ibidi chamber. Fluorescence Correlation Spectroscopy
490 (FCS) measurements were performed using Zeiss LSM 780 microscope. 488 nm argon ion laser
491 was used to excite GFP. 40x/1.2 NA water immersion objective was used to focus the light in
492 solution. 40-50 curves were taken (5 s each) in solution where PSV-GFP particles diffuse freely.
493 Laser power was set to 0.1% of the total laser power that corresponds to ≈2 µW. Curves were
494 then fitted with FoCuS-point software[34] to extract number of diffusing species and brightness of
495 single diffusing species.
496

497 **Cryo-EM sample preparation and imaging**

498 Spike trimer (1.8mg/ml) S6-P and Fu2 (2.1mg/ml) were mixed in a 1:6 molar ratio followed by
499 incubation on ice for 10 minutes. Prior to cryo-EM grid preparation, grids were glow-discharged
500 with 25 mA for 2 minutes using an EMS 100X (Electron Microscopy Sciences) glow-discharge

501 unit. CryoMatrix® holey grids with amorphous alloy film (R 2/1 geometry; Zhenjiang Lehua
502 Technology Co., Ltd) were used. 3 µl aliquots of sample solutions were applied to the grids and
503 the grids with sample were then vitrified in a Vitrobot Mk IV (Thermo Fisher Scientific) at 4°C
504 and 100% humidity (blot 10 s, blot force 3, 595 filter papers (Ted Pella Inc.)). Cryo-EM data
505 collection was performed with EPU (Thermo Fisher Scientific) using a Krios G3i transmission-
506 electron microscope (Thermo Fisher Scientific) operated at 300 kV in the Karolinska Institutet's
507 3D-EM facility (https://ki.se/cmb/3d-em). Images were acquired in 165 kx nanoprobe EFTEM
508 SA mode with a slit width of 10 eV using a K3 Bioquantum. Exposure time was 1.5 s during
509 which 60 movie frames were collected with a fluency of 0.81 e-/Å2 per frame (Table S1).
510 Motion correction, CTF-estimation, Fourier binning (to 1.01 Å/px), picking and extraction in
511 600-pixel boxes (size threshold 400 Å, distance threshold 100 Å, using the pretrained
512 BoxNet2Mask_20180918 model) were performed on the fly using Warp[35]. Due to preferential
513 orientation, we collected a part of the dataset with a 25-degree stage tilt.
514 A total of 14,081 micrographs were selected based on an estimated resolution cut-off of 4 Å and
515 defocus below 2 microns as estimated by Warp. Furthermore, Warp picked 1,035,962 particles
516 (dimer of trimeric spike with Fu2) based on above-mentioned criteria. Extracted particles were
517 imported into cryoSPARC v3.1[36] for 2D classification, 3D classification and non-uniform 3D
518 refinement. After 2D classification, clean classes with high-resolution features (and with
519 characteristic trimeric spike views) were retained and used to generate ab-initio 3D
520 reconstructions. In total 277,372 particles were retained for refinement steps and these particles
521 were processed with C1 symmetry (image processing scheme Fig. S5).
522 These particles were further processed using heterogeneous refinement that resulted in a
523 reconstruction with high-resolution structural features in the core of the spike. One round of
524 homogeneous refinement was followed by non-uniform refinement. All final reconstructions

525 were analysed using 3D-FSC [37] and there were moderate anisotropy in the full map
526 reconstructions while the localized reconstruction displayed no significant anisotropy (Fig. S6A
527 and S6B). All CTF refinements were per-particle CTF refinements interspersed with global
528 aberration correction (beamtilt, trefoil, tetrafoil and spherical aberration). Please see Table S1 for
529 data collection and processing statistics and the respective cryo-EM data processing schemes.
530 For the Spike-Fu2 dimer interface we used a particle set with partial-signal subtraction of all
531 parts except for Fu2-RBD dimer interface (containing two RBDs and two Fu2). From this we
532 performed local reconstruction (non-uniform). The local reconstruction resulted in a map with
533 2.89Å overall resolution as compared to 3.2Å overall resolution for the full map.
534

535 **Cryo-EM model building and structure refinement**

536 The structure of the spike protein trimer PDB: 7KSG[5] was used as a starting model for model
537 building. A homology model for Fu2 was generated by SWISS-MODEL[38] with PDB: 5LHN as
538 template (chain B)[39]. Structure refinement and manual model building were performed using
539 Coot[40] and PHENIX [41] in interspersed cycles with secondary structure, Ramachandran, rotamers
540 and bond geometry restrains. Structure figures and EM density-map figures were generated with
541 UCSF ChimeraX[42] and COOT, respectively. Please see Table S2 for refinement and validation
542 statistics.
543

544 **SARS-CoV-2 challenge experiments**

545 K18-hACE2 transgenic mice were purchased from Jackson laboratories and maintained as a
546 hemizygous line. Experiments were conducted in BSL3 facilities at the Comparative Medicine
547 department (KM-F) at Karolinska Institutet. Ethics for studies of virus infection and therapeutic
548 intervention were obtained from the Swedish Board of Agriculture (10513-2020). Mice were

549 administered nanobodies as described in the main text and challenged intranasally with 86 PFU
550 SARS-CoV-2 ('wild-type', Swedish isolate) or 100 PFU B.1.351 in 40 µl PBS following
551 isoflurane sedation. The challenge in Fig. S7 was performed with 1000 PFU of SARS-CoV-2
552 (Swedish isolate) propagated in Vero E6 cells. Oropharyngeal sampling was performed at the
553 indicated timepoints under light anesthesia with isoflurane. Weight and general body condition
554 were monitored daily until weight drop started, whereupon mice were monitored twice daily.
555 During the experiment, weight loss, changes in general health, breathing, body movement and
556 posture, piloerection and eye health were monitored. Mice were typically sacrificed when they
557 achieved 20% weight loss. However, some mice were sacrificed before losing 20% in body
558 weight, when movement was greatly impaired and/or they experienced difficulty breathing that
559 was considered to reach a severity level of 0.5 on Karolinska Institutet's veterinary plan for
560 monitoring animal health. The weight loss in response to infection was highly reproducible. In
561 Fig. 4 data from 50% of the challenged and untreated animals are historical controls from
562 previous experiments performed under identical conditions.
563

564 **RNA Extraction and RT-qPCR for SARS-CoV-2 detection**

565 Viral RNA was isolated from buccal swabs collected on dpi 6 and stored in 500 µl of TRIzol™
566 Reagent (Invitrogen). Total RNA extractions from buccal swab samples were performed using
567 an adapted TRIzol™ manufacturers protocol with a 45 min precipitation step at -20° C. RNA
568 pellets were resuspended in 20 µl of RNase-free water.
569 RT-PCR reactions were performed using 4 µl of resuspended RNA in a 20 µl reaction volume
570 using the Superscript III one step RT-qPCR system with Platinum Taq Polymerase (Invitrogen)
571 with 400 nM concentrations of each primer and 200 nM of probe. Primers and probes for the
572 CoV-E gene target were as previously described [43]. Primers and probes for the ABL1 target were

573 adapted from Ishige et al.[44] to enable detection of the murine homolog: (ABL1_ENF1003_deg:
574 5'-TGGAGATAACACTCTCAGCATKACTAAAGGT-3', ABL1_ENR1063: 5'-
575 GATGTAGTTGCTTGGGACCCA-3', ABL1_ENPr1043_deg: 5'-HEX-
576 CCATTTTTSGTTTGGGCTTCACACCATT-BHQ1-3'). The CoV-E and ABL1 TaqMan assays
577 were run in multiplex. Detection of the subgenomic CoV-E target was adapted from Wölfel et
578 al.[45], using a leader/E gene junction specific forward primer: (sgEjunc_SARSCoV2_F: 5'-
579 CGATCTCTTGTAGATCTGTTCTCTAAACG-3'). All oligonucleotides were synthesized by
580 Eurofins Genomics.
581 Thermal cycling conditions for all assays consisted of RT at 55 °C for 10 min, denaturation at 95
582 °C for 3 min, and 45 cycles of 95C, 15s and 58C, 30s. Reactions were carried out using a CFX96
583 Connect Real-Time PCR Detection System (Bio-Rad) following manufacturer instructions. To
584 generate standard curves, a synthetic DNA template gBlock (Integrated DNA Technologies) was
585 transcribed using the mMessage mMachine™ T7 Transcription Kit (Invitrogen) and serially
586 diluted. To reduce sampling-related variability, SARS-CoV-2 RNA copies were normalized by
587 ABL1 copies, and this ratio was used for comparisons. ABL1 copies were not significantly
588 different between groups.
589

590 **References**

591 1. Cele, S. *et al.* Escape of SARS-CoV-2 501Y.V2 from neutralization by convalescent
592 plasma. *Nature* **593**, 142–146 (2021).
593 2. Muyldermans, S. Nanobodies: Natural Single-Domain Antibodies. *Annu. Rev. Biochem.*
594 **82**, 775–797 (2013).
595 3. Moliner-Morro, A. *et al.* Picomolar SARS-CoV-2 neutralization using multi-arm PEG
596 nanobody constructs. *Biomolecules* **10**, 1–11 (2020).

597 4. Hultberg, A. *et al.* Llama-derived single domain antibodies to build multivalent,
598 superpotent and broadened neutralizing anti-viral molecules. *PLoS One* **6**, 1–12 (2011).
599 5. Koenig, P.-A. *et al.* Structure-guided multivalent nanobodies block SARS-CoV-2
600 infection and suppress mutational escape. *Science* **371**, eabe6230 (2021).
601 6. Wrapp, D. *et al.* Cryo-EM structure of the 2019-nCoV spike in the prefusion
602 conformation. *Science* **367**, (2020).
603 7. Walls, A. C. *et al.* Structure, Function, and Antigenicity of the SARS-CoV-2 Spike
604 Glycoprotein. *Cell* **181**, 281-292.e6 (2020).
605 8. Walls, A. C. *et al.* Unexpected Receptor Functional Mimicry Elucidates Activation of
606 Coronavirus Fusion. *Cell* **176**, 1026-1039.e15 (2019).
607 9. Pallesen, J. *et al.* Immunogenicity and structures of a rationally designed prefusion
608 MERS-CoV spike antigen. *Proc. Natl. Acad. Sci. U. S. A.* **114**, E7348–E7357 (2017).
609 10. Wang, C. *et al.* A human monoclonal antibody blocking SARS-CoV-2 infection. *Nat.*
610 *Commun.* **11**, 1–6 (2020).
611 11. Liu, L. *et al.* Potent neutralizing antibodies against multiple epitopes on SARS-CoV-2
612 spike. *Nature* **584**, 450–456 (2020).
613 12. Lei, C. *et al.* Neutralization of SARS-CoV-2 spike pseudotyped virus by recombinant
614 ACE2-Ig. *Nat. Commun.* **11**, (2020).
615 13. Custódio, T. F. *et al.* Selection, biophysical and structural analysis of synthetic nanobodies
616 that effectively neutralize SARS-CoV-2. *Nat. Commun.* **11**, (2020).
617 14. Hanke, L. *et al.* An alpaca nanobody neutralizes SARS-CoV-2 by blocking receptor
618 interaction. *Nat. Commun.* **11**, 4420 (2020).
619 15. Xiang, Y. *et al.* Versatile and multivalent nanobodies efficiently neutralize SARS-CoV-2.
620 *Science* **370**, 1479–1484 (2021).

621 16. Schoof, M. *et al.* An ultrapotent synthetic nanobody neutralizes SARS-CoV-2 by
622 stabilizing inactive Spike. *Science* **370**, 1473–1479 (2021).
623 17. Ibañez, L. I. *et al.* Nanobodies with in vitro neutralizing activity protect mice against
624 H5N1 influenza virus infection. *J. Infect. Dis.* **203**, 1063–1072 (2011).
625 18. Wang, Q. *et al.* Structural and Functional Basis of SARS-CoV-2 Entry by Using Human
626 ACE2. *Cell* **181**, 894-904.e9 (2020).
627 19. Monteil, V. *et al.* Inhibition of SARS-CoV-2 Infections in Engineered Human Tissues
628 Using Clinical-Grade Soluble Human ACE2. *Cell* **181**, 905-913.e7 (2020).
629 20. Roovers, R. C. *et al.* A biparatopic anti-EGFR nanobody efficiently inhibits solid tumour
630 growth. *Int. J. Cancer* **129**, 2013–2024 (2011).
631 21. Cardoso, F. M. *et al.* Single-Domain Antibodies Targeting Neuraminidase Protect against
632 an H5N1 Influenza Virus Challenge. *J. Virol.* **88**, 8278–8296 (2014).
633 22. Power, U. F., Stortelers, C., Allosery, K. & Melero, J. A. Generation and Characterization
634 of ALX-0171 , a Potent Novel Therapeutic Nanobody for the Treatment of Respiratory
635 Syncytial Virus Infection. *Antimicrob. Agents Chemother.* **60**, 6–13 (2016).
636 23. Planas, D. *et al.* Sensitivity of infectious SARS-CoV-2 B.1.1.7 and B.1.351 variants to
637 neutralizing antibodies. *Nat. Med.* 1–8 (2021) doi:10.1038/s41591-021-01318-5.
638 24. Tada, T. *et al.* Neutralization of viruses with European, South African, and United States
639 SARS-CoV-2 variant spike proteins by convalescent sera and BNT162b2 mRNA vaccine-
640 elicited antibodies. *bioRxiv Prepr. Serv. Biol.* 2021.02.05.430003 (2021)
641 doi:10.1101/2021.02.05.430003.
642 25. Hu, J. *et al.* Emerging SARS-CoV-2 variants reduce neutralization sensitivity to
643 convalescent sera and monoclonal antibodies. *Cell. Mol. Immunol.* 1–3 (2021)
644 doi:10.1038/s41423-021-00648-1.

645 26. Wrapp, D. *et al.* Structural Basis for Potent Neutralization of Betacoronaviruses by
646 Single-Domain Camelid Antibodies. *Cell* **181**, 1004-1015.e15 (2020).
647 27. Schepens, B. *et al.* Drug development of an affinity enhanced, broadly neutralizing heavy
648 chain-only antibody that restricts SARS-CoV-2 in hamsters. *bioRxiv* 2021.03.08.433449
649 (2021) doi:10.1101/2021.03.08.433449.
650 28. Cortez-Retamozo, V. *et al.* Efficient tumor targeting by single-domain antibody fragments
651 of camels. *Int. J. Cancer* **98**, 456–462 (2002).
652 29. Vieira, P. & Rajewsky, K. The half-lives of serum immunoglobulins in adult mice. *Eur. J.*
653 *Immunol.* **18**, 313–316 (1988).
654 30. Bangaru, S. *et al.* Structural analysis of full-length SARS-CoV-2 spike protein from an
655 advanced vaccine candidate. *Science* **370**, 1089–1094 (2020).
656 31. Hanke, L. *et al.* The Antiviral Mechanism of an Influenza A Virus Nucleoprotein-Specific
657 Single-Domain Antibody Fragment. *MBio* **7**, e01569--16 (2016).
658 32. Song, W., Gui, M., Wang, X. & Xiang, Y. Cryo-EM structure of the SARS coronavirus
659 spike glycoprotein in complex with its host cell receptor ACE2. *PLoS Pathog.* **14**, (2018).
660 33. Hsieh, C. L. *et al.* Structure-based design of prefusion-stabilized SARS-CoV-2 spikes.
661 *Science* **369**, 1501–1505 (2020).
662 34. Waithe, D., Clausen, M. P., Sezgin, E. & Eggeling, C. FoCuS-point: Software for STED
663 fluorescence correlation and time-gated single photon counting. *Bioinformatics* **32**, 958–
664 960 (2016).
665 35. Tegunov, D. & Cramer, P. Real-time cryo-electron microscopy data preprocessing with
666 Warp. *Nat. Methods* **16**, 1146–1152 (2019).
667 36. Punjani, A., Rubinstein, J. L., Fleet, D. J. & Brubaker, M. A. CryoSPARC: Algorithms for
668 rapid unsupervised cryo-EM structure determination. *Nat. Methods* **14**, 290–296 (2017).

669 37. Zi Tan, Y. *et al.* Addressing preferred specimen orientation in single-particle cryo-EM
670 through tilting. *Nat. Methods* **14**, 793–796 (2017).
671 38. Waterhouse, A. *et al.* SWISS-MODEL: Homology modelling of protein structures and
672 complexes. *Nucleic Acids Res.* (2018) doi:10.1093/nar/gky427.
673 39. Kromann-Hansen, T. *et al.* Discovery of a novel conformational equilibrium in urokinase-
674 type plasminogen activator. *Sci. Rep.* **7**, 1–11 (2017).
675 40. Emsley, P., Lohkamp, B., Scott, W. G. & Cowtan, K. Features and development of Coot.
676 *Acta Crystallogr. Sect. D Biol. Crystallogr.* **66**, 486–501 (2010).
677 41. Adams, P. D. *et al.* PHENIX: A comprehensive Python-based system for macromolecular
678 structure solution. *Acta Crystallogr. Sect. D Biol. Crystallogr.* **66**, 213–221 (2010).
679 42. Goddard, T. D. *et al.* UCSF ChimeraX: Meeting modern challenges in visualization and
680 analysis. *Protein Sci.* **27**, 14–25 (2018).
681 43. Corman, V. M. *et al.* Detection of 2019 novel coronavirus (2019-nCoV) by real-time RT-
682 PCR. *Eurosurveillance* **25**, 2000045 (2020).
683 44. Ishige, T. *et al.* Highly sensitive detection of SARS-CoV-2 RNA by multiplex rRT-PCR
684 for molecular diagnosis of COVID-19 by clinical laboratories. *Clin. Chim. Acta* **507**, 139–
685 142 (2020).
686 45. Wölfel, R. *et al.* Virological assessment of hospitalized patients with COVID-2019.
687 *Nature* **581**, 465–469 (2020).
688 46. Tortorici, M. A. *et al.* Ultrapotent human antibodies protect against SARS-CoV-2
689 challenge via multiple mechanisms. *Science* **370**, 950–957 (2020).
690 47. Benton, D. J. *et al.* Receptor binding and priming of the spike protein of SARS-CoV-2 for
691 membrane fusion. *Nature* **588**, 327–330 (2020).
692 48. Zhou, T. *et al.* A pH-dependent switch mediates conformational masking of SARS-CoV-2

693 spike. *bioRxiv Prepr. Serv. Biol.* 2020.07.04.187989 (2020)
694 doi:10.1101/2020.07.04.187989.
695 49. Chen, V. B. *et al.* MolProbity: All-atom structure validation for macromolecular
696 crystallography. *Acta Crystallogr. Sect. D Biol. Crystallogr.* **66**, 12–21 (2010).
697 50. Barad, B. A. *et al.* EMRinger: Side chain-directed model and map validation for 3D cryo-
698 electron microscopy. *Nat. Methods* **12**, 943–946 (2015).
699

Acknowledgments: Experiments with replication-competent SARS-CoV-2 were performed in the Biomedicum BSL3 core facility, Karolinska Institutet. We thank Jonas Klingstrom for providing Calu-3 cells and sharing the Swedish SARS-CoV-2 isolate, and Alex Sigal from the Africa Health Research Institute for providing the B.1.351/501Y.V2 isolate. All cryo-EM data were collected in the Karolinska Institutet's 3D-EM facility. We thank Agustin Ure for assistance with figure generation and Tomas Nyman (Protein Science Facility at KI) for providing access to SPR instruments.

Funding: LH was supported by the David och Astrid Hageléns stiftelse, the Clas Groschinskys Minnesfond and a Jonas Söderquist's scholarship. This project has received funding from the European Union's Horizon 2020 research and innovation program under grant agreement No. 101003653 (CoroNAb), to BM and GMM. BMH is supported by the Knut and Alice Wallenberg Foundation (KAW 2017.0080 and KAW 2018.0080). The work was supported by project grants from the Swedish Research Council to BMH (2017-6702 and 2018-3808), BM (2018-02381) and to GMM (2018-03914 and 2018-03843).

Author contributions: Conceptualization: LH, BM, GMM. Methodology: LH, DJS, JMC, BMH, BM, GMM. Investigation: LH, HD, DJS, LPV, EU, AMM, VK, BP, ES, NS, AP, CK, GKP, BMH. Data Curation: LH, BM. Visualization: LH, HD, DJS, BMH, BM. Funding acquisition: LH, BMH, BM, GMM. Supervision: LH, DJS, OFC, JMC, BMH, BM, GMM. Writing – original draft: LH, HD. Writing – review & editing: LH, HD, DJS, LPV, EU, AMM, VK, ES, GKP, JMC, BMH, BM, GMM.

Competing interests: LH, DJS, LPV, BM, and GMM are listed as inventors on a patent application describing SARS-CoV-2 nanobodies.

Data and materials availability: The cryo-EM density maps have been deposited in the Electron Microscopy Data Bank under accession codes EMD-12561 (dimer of spike trimer + 6 Fu2) and EMD-12465 (localized reconstruction of 2 RBDs + 2 Fu2). The atomic coordinates have been deposited in the Protein Data Bank under IDs 7NS6 (dimers of spike trimers + 6 Fu2) and 7NLL (localized reconstruction of 2 RBDs + 2 Fu2). All nanobody sequences will be made available on public databases upon publication.

Supplementary figures and tables

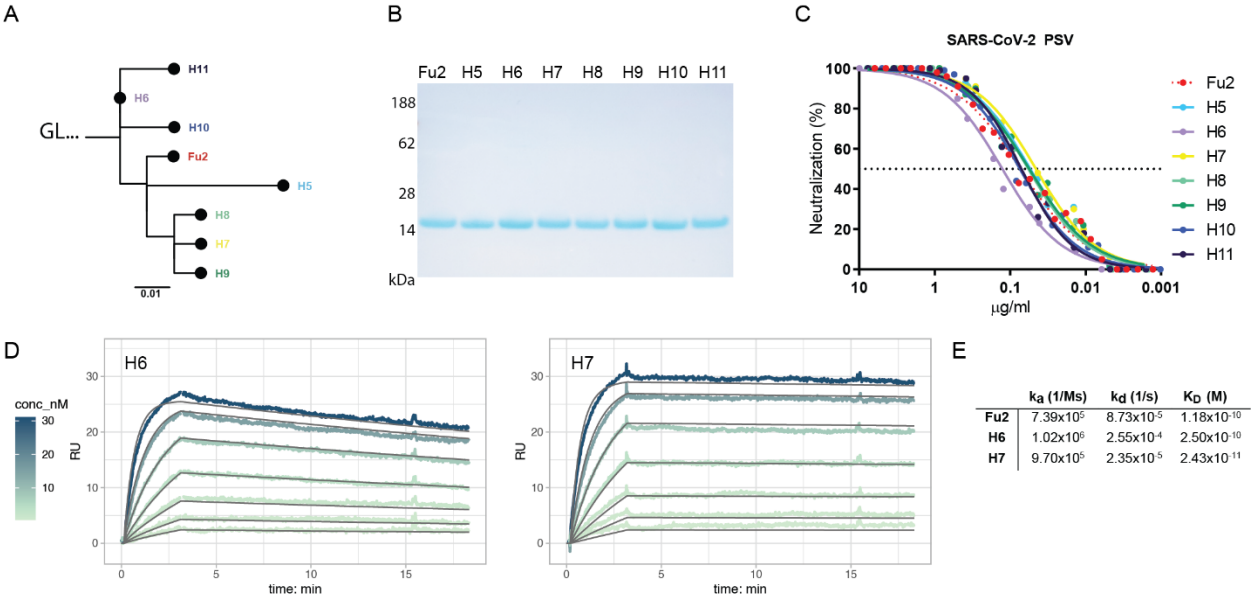

	k_a (1/Ms)	k_d (1/s)	K_D (M)
Fu2	7.39×10^{5}	8.73×10^{-5}	1.18×10^{-10}
H6	1.02×10^{6}	2.55×10^{-4}	2.50×10^{-10}
H7	9.70×10^{5}	2.35×10^{-5}	2.43×10^{-11}

Fig. S1. Fu2 variants identified by next-generation sequencing (NGS) display similar neutralization potential and binding kinetics. (**A**) Average difference of Fu2 variants is shown as a tree diagram. (**B**) Fu2 and seven Fu2-variants were expressed in *E. coli*, purified, and analyzed by SDS-PAGE and Coomassie staining. (**C**) A dilution series of Fu2 and its variants were incubated with SARS-CoV-2 pseudotyped lentivirus (PSV) for 1 hour at 37 °C before infecting HEK293T-hACE2 cells. Neutralization (in %) compared to the untreated PSV is shown. (**D**) Binding kinetics of Fu2 and variants to the RBD were measured by surface plasmon resonance (SPR). Site-specifically biotinylated RBD was immobilized on streptavidin sensor chips, and kinetics for a dilution series of the indicated monomeric nanobodies were measured. Sensorgrams are color-coded based on concentration. The fit is based on the 1:1 Langmuir model and is shown in dark grey solid lines. (**E**) Kinetic parameters of Fu2 and Fu2 variants binding to the RBD.

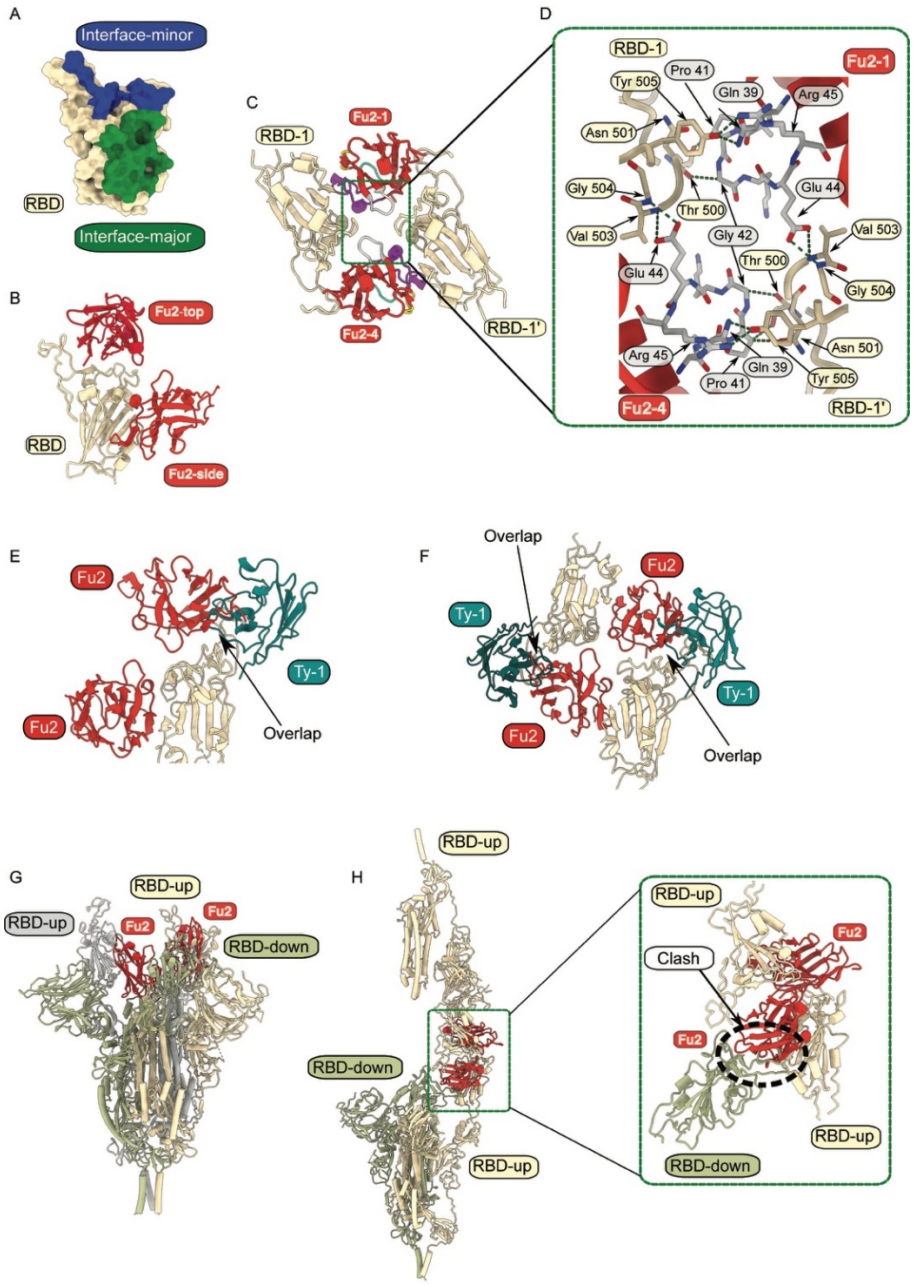

Fig. S2. (**A**) Surface view of the RBD with interface-major and interface-minor color coded. (**B**) Relative positions of two Fu2 molecules binding the RBD. (**C**) The interaction between two RBDs and two Fu2s showing in grey the β-hairpins in the Fu2 framework region (39-45) that help to mediate the dimer-of-trimers Fu2-spike complex. (**D**) Close-up view of (C) (**E** and **F**) Assessment of Fu2-Ty1 heterodimer binding. Alignment of the Spike-Fu2 structure to the Spike-Ty1 structure (RBD in 'up' conformation) (PDB:6ZXN[14]). Arrows indicate partial overlap of binding surface on RBD**.** (**G**) Assessment of Fu2-RBD interaction in RBD-down conformation. RBD-Fu2 structure superimposed to RBD-down of spike in 2-up conformation (PDB:7A29) (**H**) Assessment of Fu2-RBD interaction in RBD-down conformation in dimeric spike. 2-up spike (PDB:7A29[13]) is shown superimposed with the spike dimer-of-trimers.

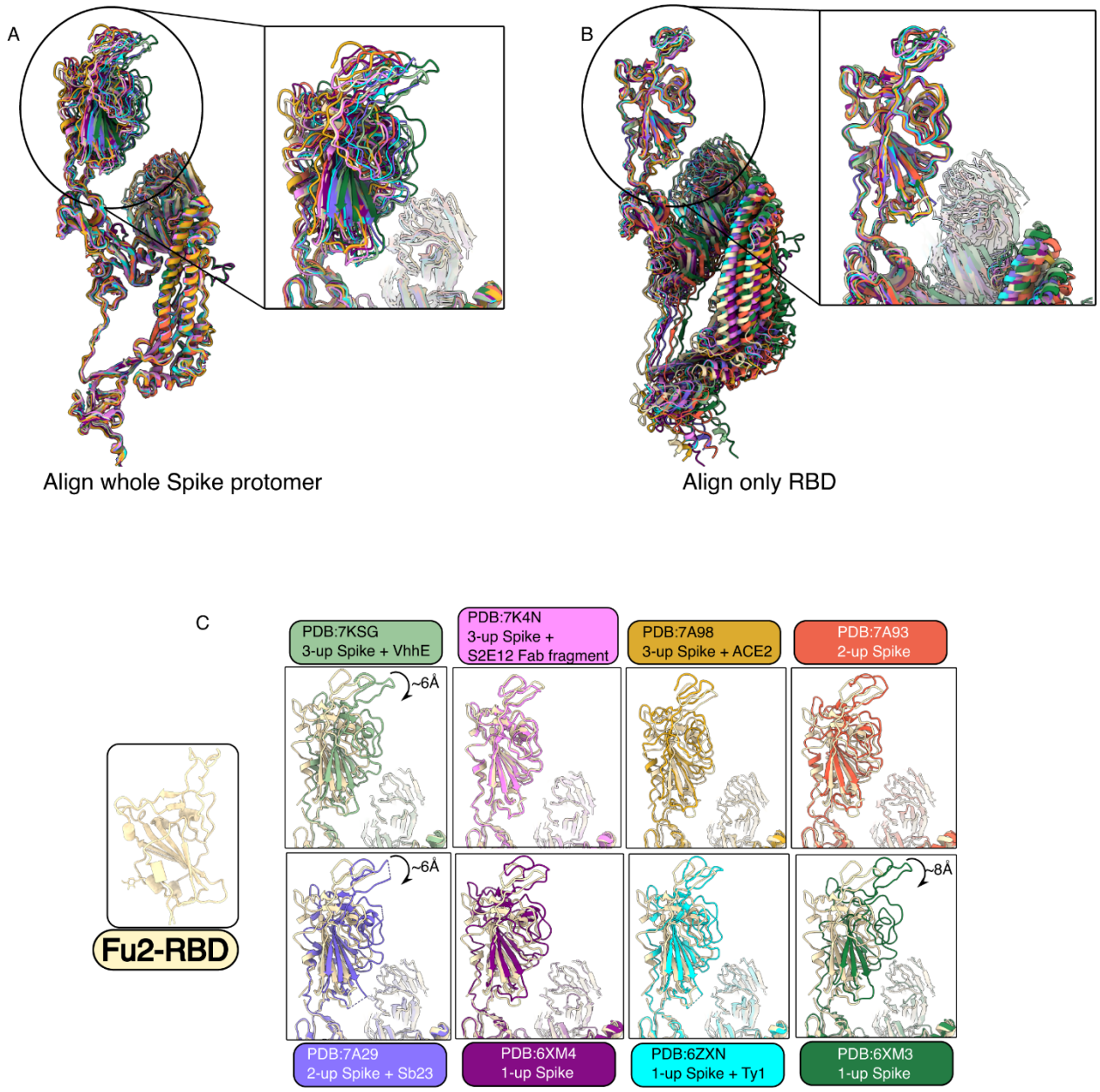

Fig. S3. Assessment of Fu2 mediated structural changes in spike structure. (**A**) Alignment of dimeric spike trimer with spikes in 1-up, 2-up and 3-up conformation (one protomer in 'up' state shown). (**B**) Structural alignment of dimeric spike trimer with RBDs of 1-up, 2-up and 3-up spikes (protomer in 'up' conformation). (**C**) Structural comparison of RBD (Fu2-bound dimeric spike) with eight different RBDs structures (7KSG[5], 7K4N[46], 7A98[47], 7A93[47], 7A29[13], 6XM3[48], 6XM4[48], 6ZXN[14]).

A

```
SARS-CoV-2 RBD  333 TNLCPFGEVFNATRFASVYAWNRKRISNCVADYSVLYNSASFSTFKCYGVSPTKLNDLCF  392
  SARS-CoV RBD  320 TNLCPFGEVFNATKFPSVYAWERKKISNCVADYSVLYNSTFFSTFKCYGVSATKLNDLCF  379
                    *************:* *****:**:**************: ********** ********

SARS-CoV-2 RBD  393 TNVYADSFVIRGDEVRQIAPGQTGKIADYNYKLPDDFTGCVIAWNSNNLDSKVGGNYNYL  452
  SARS-CoV RBD  380 SNVYADSFVVKGDDVRQIAPGQTGVIADYNYKLPDDFMGCVLAWNTRNIDATSTGNYNYK  439
                    :********::**:********** ************ ***:***:.*:*:.  *****

SARS-CoV-2 RBD  453 YRLFRKSNLKPFERDISTEIYQAGSTPC GVEGFNCYFPLQSYGFQPTNGVGYQPYRVVV  512
  SARS-CoV RBD  440 YRYLRHGKLRPFERDISNVPFSPDGKPCT-PPALNCYWPLNDYGFYTTTGIGYQPYRVVV  499
                    ** :*:.:*:*******.  :. ...**.   .:***:**:.***  *.*:*********

SARS-CoV-2 RBD  513 LSFELLHAPATVCGPK  514
  SARS-CoV RBD  500 LSFELLNAPATVCGPK  528
                    ******:*********
```

residues interface-major

residues interface-minor

B

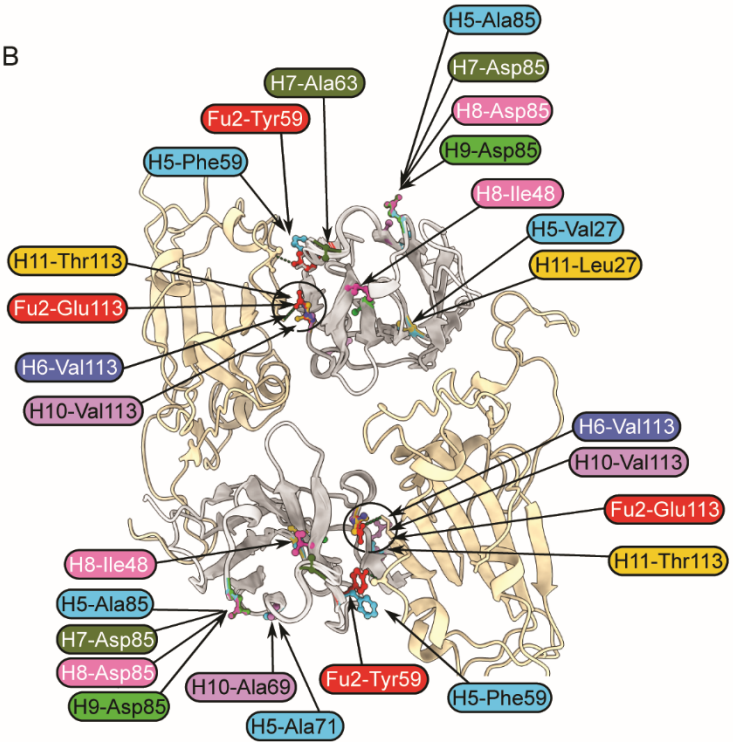

Fig. S4. (**A**) Sequence alignment of RBDs from SARS-CoV and SARS-CoV-2. Interface-major and interface-minor residues are highlighted. Arrows indicate the different amino acids of the interface. (**B**) Fu2 variants and analysis of interface residues. Distinct residues of different variants shown as sticks (color coded).

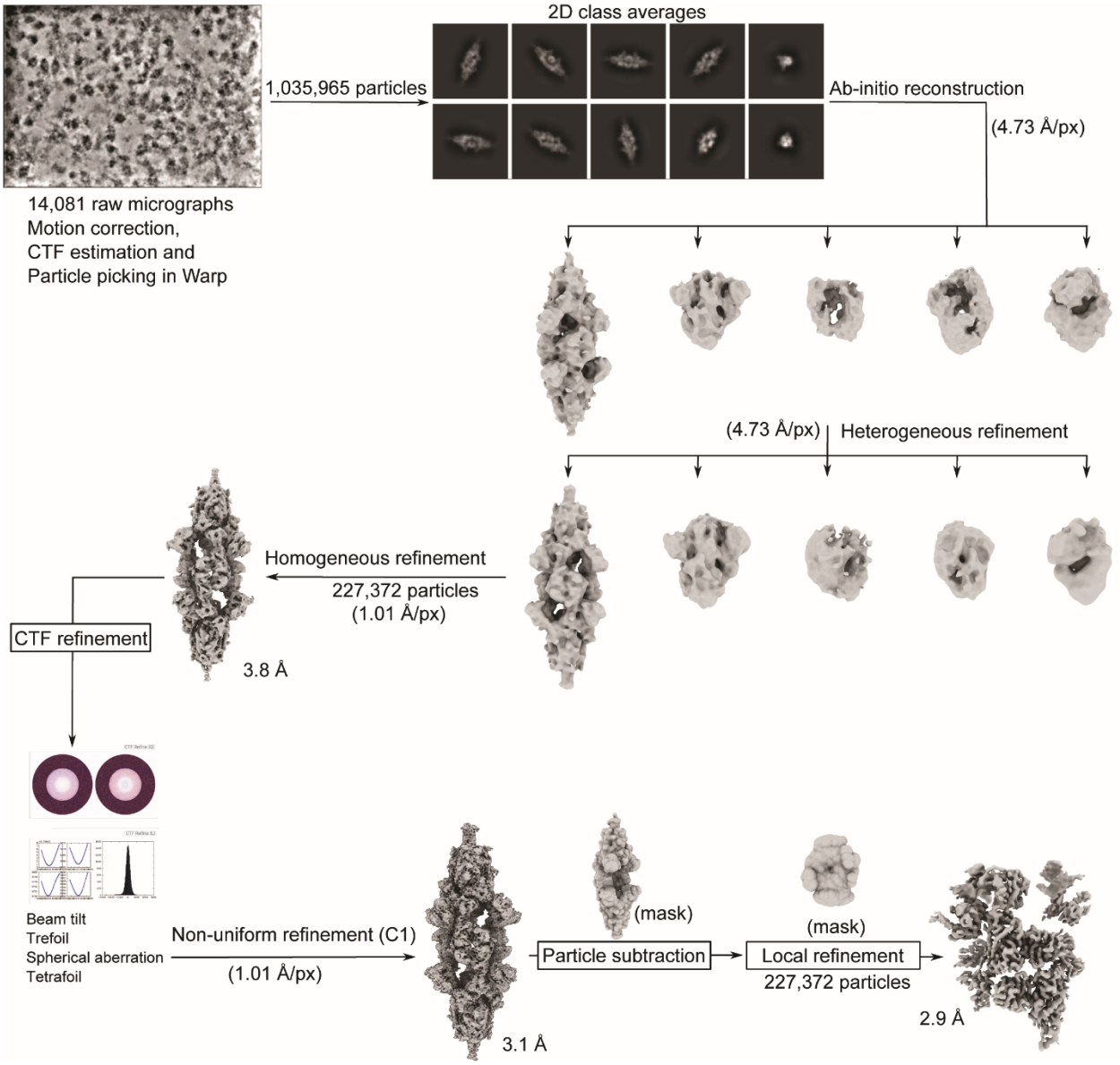

Fig. S5 Cryo-EM image processing scheme. Particles picked by Warp[35] were processed in cryoSPARC v3.1[36]. Representative 2D class averages are shown. Particles contributing to the clean classes were used to generate ab-initio reconstructions (five classes) followed by heterogeneous refinement. One class showing high-resolution features was refined further (C1 symmetry). For localized reconstruction, particle subtraction followed by local refinement (Non-uniform) was performed.

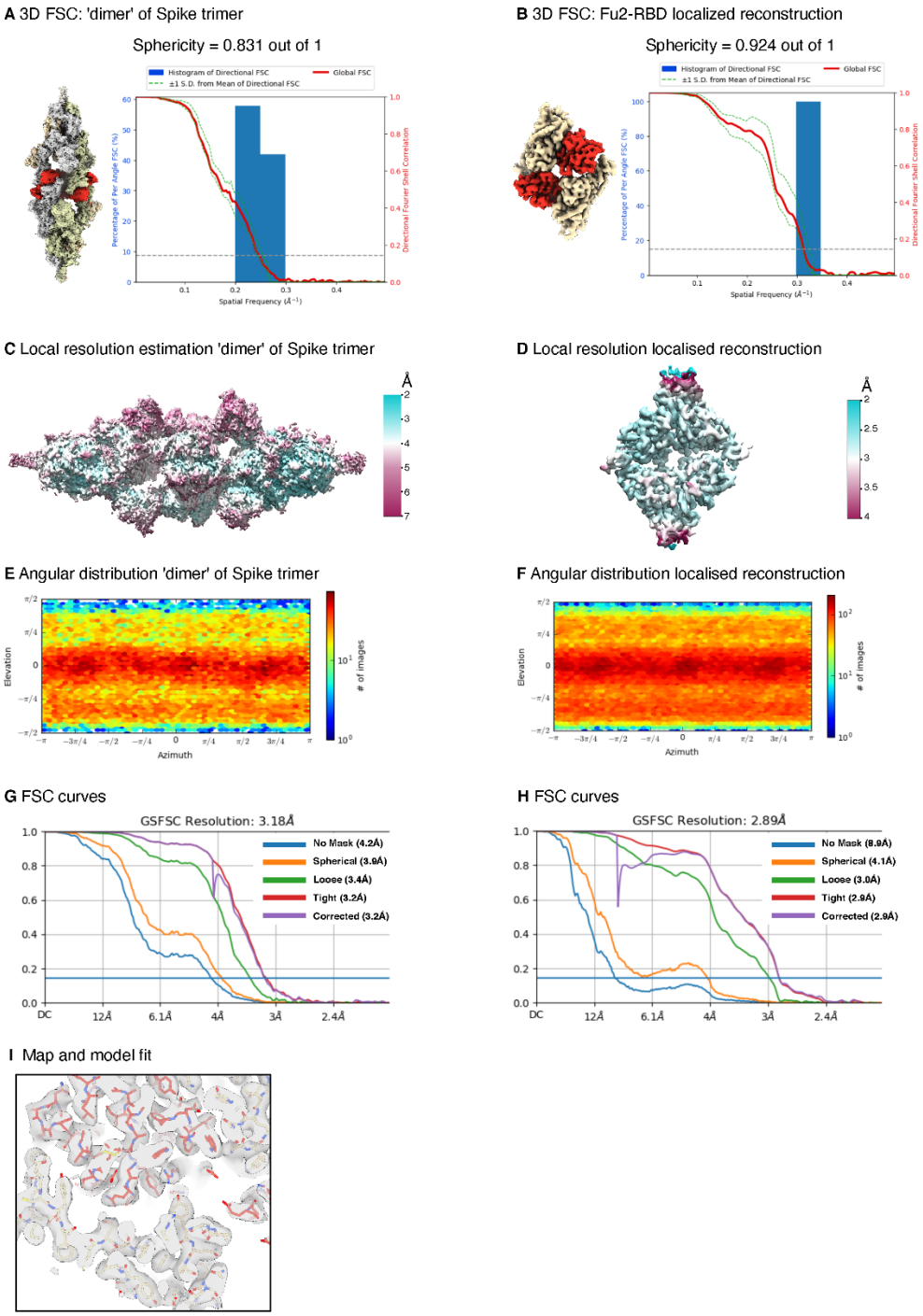

Fig. S6 Cryo-EM validation (**A**) and (**B**) 3D FSC[37] and sphericity of 'dimer' of spike trimer and of localized map, (**C**) and (**D**) Local resolution estimation of 'dimer' of spike trimer and local resolution estimation of localized map (**E**) and (**F**) Angular distribution of 'dimer' of spike trimer reconstruction and localized reconstruction map (**G**) and (**H**) FSC curves of 'dimer' of spike trimer and of localized map (**I**) model-map fitting atomic resolution.

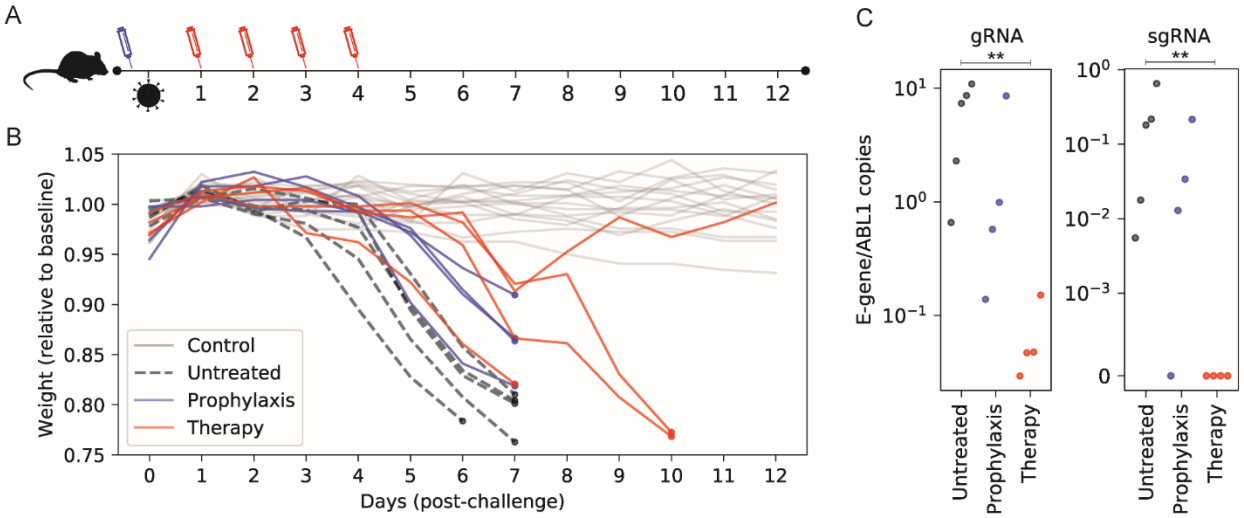

Fig. S7. Non-half-life extended nanobody heterodimer reduces disease severity in a SARS-CoV-2 challenge model.

(**A**) Timeline of the challenge experiment. K18-hACE2 transgenic mice were challenged with 1000 plaque forming units (PFU) of SARS-CoV-2 (Swedish isolate) and received prophylactic (blue) or therapeutic (red) Fu2-Ty1 at the indicated time points. (**B**) Weight of mice during the challenge experiment. The mean weight of each mouse of day 0 to day 2 served as baseline and the weight loss relative this baseline is shown. Uninfected mice are shown in grey, untreated infected mice in black, prophylactic treatment group in blue and therapeutic group in red. (**C**) Analysis of oropharyngeal samples from mice at day 6 in infected groups. Ratios of E-gene to ABL1 is shown for both genomic and subgenomic RNA (** $p < 0.01$, Mann–Whitney U test, one-tailed).

822 **Table S1. Cryo-EM data collection and processing**

823

	Dimer of spike trimer + 6 Fu2	Localized reconstruction of 2 RBDs + 2 Fu2
EMDB	**EMD-12561**	**EMD-12465**
PDB	**7NS6**	**7NLL**
Data collection		
Microscope	TFS Krios G3i	
Voltage (kV)	300	
Detector	Bioquantum K3	
Recording mode	Counting	
EFTEM SA Magnification	165kx	
Calibrated pixel size (Å)	0.505	
Movie micrograph pixel size (Å)	0.505	
Flux (e^-/[(camera pixel)*s])	8.4	
Number of frames per movie micrographs	60	
Total movie micrograph exposure time (s)	1.5	
Fluency (e^-/Å^2)	48.6	
Underfocus range (µm)	0.2 – 1.3	
Energy filter slit width (eV)	10	
Data collection automation software	EPU	
EM Data processing		
Number of micrographs	14,081	14,081
Number of total projection images	1,035,962	1,035,962
Number of projection images used for reconstruction	277,372	277,372
Symmetry	C1	C1
Map resolution (FSC 0.143; Å)	3.18	2.9
Map resolution no mask (FSC 0.143; Å)	4.2	8.9
B-factor applied to map (Å^2)	68.1	37.3
3D-FSC[37]		
3D-FSC resolution (3D-FSC 0.143; Å)	4.0	3.2
Sphericity (3D-FSC)	0.831	0.924

824

825 **Table S2. Cryo-EM model refinement and validation statistics**
826

	Dimer of spike trimers + 6 Fu2	Localized reconstruction of 2 RBDs + 2 Fu2
EMDB	**EMD-12561**	**EMD-12465**
PDB	**7NS6**	**7NLL**
Refinement		
Refinement Package	PHENIX 1.19	PHENIX 1.19
Refinement space	Real	Real
Highest resolution used	3.2	2.9
Model composition		
Atoms refined	55904	5058
Residues SARS-CoV-2 Spike (or RBD) and nanobody Fu2	7109	656
Glycans	50	2
Full Map-model correspondence		
Map correlation coefficient	0.87	0.90
Map to model FSC (Å) (FSC 0.143)	3.2	2.6
Mean B-factor		
Residues SARS-CoV-2 Spike (or RBD) and nanobody Fu2	140	85.89
Glycans	129	96.22
Model geometry		
RMSD ideal bond length (Å)	0.004	0.003
RMSD ideal bond angles (˚)	0.826	0.529
Side chain rotamer outliers (%)	0	0
C-ß outliers (%)	0.38	0
Ramachandran plot		
Favored (%)	97.76	99.38
Outliers (%)	0	0
General macromolecular model validation		
MolProbity score[49]	1.66	1.38
Clashscore[49]	12.38	6.92
EM specific model validation		
CaBLAM (%)[50]	2.55	0.94
EM-ringer score[50]	1.73	3.16

827
828